Intraseasonal transition of Northern Hemisphere planetary waves and the underlying mechanism during the abrupt-change period of early summer

Zuowei Xie[1] · Bueh Cholaw[1] · Yi Deng[2] · Bian He[3] · Sheng Lai[1,4]

Abstract

Northern Hemisphere planetary waves exhibit an abrupt change in early summer and a significant impact on East Asian summer monsoon rainfall. Although great achievements have been made toward understanding the characteristics and maintenance of planetary waves during winter and summer, the transition of planetary waves during the abrupt-change period is less well understood. This study aims to assess the relative contribution of harmonic waves to the planetary wave transition and mechanism from the perspective of full nonlinear responses to the mountains of Asia (above 500 m) during May and June, with a primary focus on the largest positive geopotential height anomaly over northeastern Asia. The largest positive geopotential height anomaly over northeastern Asia is primarily contributed by wavelengths of around 7000 km, which corresponds to zonal wavenumber 3. The mid–high latitudes planetary waves mainly consist of wavelengths of around 10,000 km (zonal wavenumber 2, roughly) and 7000 km, which are in-phase (out-of-phase) with each other over the Western (Eastern) Hemisphere. Wavelengths of around 10,000 km weaken and displace eastward, while those of 7000 km magnify and hence contribute to the largest positive geopotential height anomaly over northeastern Asia. The full nonlinear response to the forcing by the mountains of Asia provides a considerable contribution to the largest geopotential height anomaly over northeastern Asia. Such a positive contribution comes mainly from the full nonlinear response to sensible heating associated with the mountains over Asia, which is partially offset by the full nonlinear response to dynamical forcing of the Asian mountains.

Keywords Planetary waves · Abrupt change · Northeastern Asia · GMMIP · Harmonic analysis

1 Introduction

Stationary waves, also known as stationary eddies, often refer to the zonally asymmetric anomalies of the time-averaged atmospheric circulation (Held et al. 2002; Nigam and DeWeaver 2015). The asymmetric features of stationary waves are rooted in the asymmetries of the lower boundary conditions, such as land–ocean contrasts and mountain terrain. Stationary waves can also be derived from the daily meteorological field using a spatiotemporal spectral analysis (Hayashi 1977; Watt-Meyer and Kushner 2015). Such daily stationary waves fluctuate in amplitude from day to day and are also referred to as planetary waves, which are considered as small wavenumbers of atmospheric waves (Holton and Mass 1976; Hayashi 1977). Planetary waves not only contribute directly to meridional fluxes of momentum and heat, but also act as a background flow providing energy for the barotropic and baroclinic instabilities of both extreme weather systems and teleconnection patterns (Charney 1947; Eady 1949; Simmons et al. 1983; Li and Ji 1997; Xie et al. 2019).

Planetary waves exhibit a drastic change during the transition seasons between winter and summer (Ye et al. 1958; Tao et al. 1958; Ting et al. 2001). The abrupt change in June

✉ Zuowei Xie
xiezuowei@mail.iap.ac.cn

1 International Center for Climate and Environment Sciences, Institute of Atmospheric Physics, Chinese Academy of Sciences, Beijing 100029, China

2 School of Earth and Atmospheric Sciences, Georgia Institute of Technology, Atlanta, GA 30332, USA

3 State Key Laboratory of Numerical Modeling for Atmospheric Sciences and Geophysical Fluid Dynamics, Institute of Atmospheric Physics, Chinese Academy of Sciences, Beijing 100029, China

4 Present Address: Climate Center of Guangxi Zhuang Autonomous Region, Nanning, Guangxi 530022, China

is more evident than that in October and concurrent with the onset of the well-known "plum rainfall" over central China and Japan (Ye et al. 1958). During this period from May to June, Chyi et al. (2021) showed that the largest change in planetary waves in the Northern Hemisphere is characterized by a warm high anomaly over northern Asia. The onset timing of such anticyclonic anomalies exerts a significant influence on the position and amount of plum rainfall over central China (Chen et al. 2021; Chyi et al. 2021). Aside from the significant climate and weather impacts of this abrupt change in June, it is hugely challenging for atmospheric global climate models to simulate. For instance, Ting et al. (2001) showed that the lowest performance of the Geophysical Fluid Dynamics Laboratory general circulation model in simulating the mid-level tropospheric planetary waves occurs during May and June.

Harmonic decomposition of planetary waves has revealed that large-scale fluctuations in boreal winter primarily consist of westward (e.g. zonal wavenumbers 1–2) and eastward (e.g. zonal wavenumber 4) propagating planetary waves (Pratt and Wallace 1976). Similar to the change in zonal wavenumber, Sun et al. (2019) discovered an apparent change in the meridional structure of planetary waves from winter to summer by applying harmonic analysis to both zonal and meridional waves. Xie et al. (2017) isolated daily planetary waves using spherical harmonic analysis and decomposed winter planetary waves into six groups based on the cluster-mean daily planetary waves. Considering the abrupt change of Northern Hemisphere circulation during the period from May to June with the largest positive geopotential height over northeastern Asia, the contributions of harmonic waves and how planetary wave patterns vary remain unclear.

Orography, diabatic heating, transient eddy and nonlinear interactions among them jointly form planetary waves (Charney and Eliassen 1949; Ting et al. 2001; Held et al. 2002). The seminal paper by Charney and Eliassen (1949) revealed the vital role of midlatitude mountains in determining the planetary wave of 45°N using a linear shallow-water model. Much of the literature using linear models has given us a tremendous wealth of knowledge regarding the relative contributions of topography, diabatic heating, and transient eddies to planetary waves (e.g. Hoskins and Karoly 1981; Ting and Held 1990). However, Ting et al. (2001) and Held et al. (2002) emphasized an important role of the nonlinear wave-wave interactions among the waves forced by orography, diabatic heating and transient eddies in planetary waves, which contributes more to winter than summer planetary waves. This nonlinearity is primarily contributed by the interaction between the flows forced by diabatic heating and orography and generates an anticyclonic circulation around Lake Baikal in summer. Chang (2009) showed that

extratropical (north of 25° N) diabatic heating and Tibetan Plateau forcings explain most of the planetary waves in model simulations. Garfinkel et al. (2020) illustrated that the strength of a planetary wave response to a given forcing depends on the background-state temperature field set by each forcing. As pointed out by Held et al. (2002), prior studies have mainly analyzed the response to heat sources as obtained from observations or general circulation models, rather than first determining the diabatic heating distribution generated from the lower boundary conditions. Although some studies have proposed a driving air-pump mechanism of the sensible heating determined by the Tibetan Plateau, they focused on its role in regulating the East Asian monsoon circulation (Wu et al. 2007; He et al. 2019b).

In spite of the great achievements regarding the characteristics and maintenance mechanism of planetary waves in the winter and summer seasons, there remains several open questions with respect to the intraseasonal variability of planetary waves and the underlying mechanisms, especially regarding the abrupt change during June, with the largest positive geopotential height anomaly over northeastern Asia. The specific questions that the current study seeks to address are as follows:

(1) How do planetary waves of different wavelength contribute to the intraseasonal change in planetary waves from May to June?
(2) How many types of planetary wave pattern are there from May to June?
(3) To what extent do the full nonlinear responses to the mountains over Asia contribute to the intraseasonal change of planetary waves from May to June?

Since the maintenance of planetary waves is separated into the Sverdrup regime in the tropics and the Rossby regime in the mid–high latitudes (Chen 2005), we restrict our attention to the mid–high latitudes to answer these three questions. This study refers planetary waves to the 500-hPa geopotential height (Z500), including the latitudinal shear of zonal mean Z500. We decompose the planetary waves over the latitudinal belt encompassing the largest positive geopotential height anomaly into different wavelengths using Morlet wavelet analysis to assess the relative contribution of each wavelength. Meanwhile, using a self-organizing map (SOM), we classify daily planetary waves during May and June into four clusters and then construct the planetary wave patterns based on the cluster-mean planetary waves. To reveal the mechanism underlying the intraseasonal change in planetary waves, we adopt Global Monsoons Model Intercomparison Project (GMMIP) Tier-3 experiments to probe the relative roles of sensible heating and dynamical forcing associated with the mountains of Asia (above 500 m).

The structure of the paper is as follows: Sect. 2 describes the data and methods; Sect. 3 presents the intraseasonal variabilities of planetary waves; Sect. 4 discusses the responses of planetary waves to Asian mountain forcing; and Sect. 5 provides a summary of the key findings and some further discussion.

2 Data and methods

2.1 Reanalysis data

We use the ERA5 global reanalysis datasets provided by the European Center for Medium-range Weather Forecasts (Hersbach et al. 2020). We obtain hourly and monthly 500-hPa geopotential on a regular 2.5° longitude–latitude grid. The daily mean Z500 is derived by averaging the hourly data divided by 9.8 m s^{-2}. Since the outputs of the GMMIP Tier-3 experiments are available over 1979–2014, we adopt the ERA5 reanalysis data for the same time period. The transitional season in this study refers to the period from 1 May to 30 June of each year (61 days).

2.2 CMIP6 data

The Chinese Academy of Sciences' Flexible Global Ocean–Atmosphere–Land System model (FGOALS-f3-L) model is participating in phase 6 of the Coupled Model Intercomparison Project (CMIP6) and has already carried out the historical Atmospheric Model Intercomparison Project (AMIP) simulation and GMMIP Tier-3 experiments (He et al. 2019a, 2020). We use the AMIP r1i1p1f1 simulation as a control result, in which the model integrates from 1 January 1970 using the observational SST and sea-ice concentration and provides the outputs over 1979–2014 for analysis. In terms of sensitivity experiments, we chose an orographic
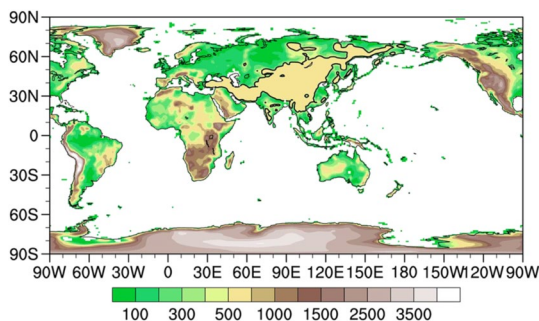
Fig. 1 Topography heights (shaded; unit: m) in the no TIP topography experiment. The thick contours are 500 m and denote the modified topography

perturbation experiment that removes the topography above 500 m over Asia (TIP; Fig. 1) and a thermal perturbation experiment that removes the sensible heating topography above 500 m in the Asian continent (TIP_nosh). In these two experiments, the model integration also starts on 1 January 1970, similar to the AMIP r1i1p1f1 simulation.

The simulated daily and monthly geopotential height data from FGOALS-f3-L are obtained from the data portals of the Earth System Grid Federation. To be more comparable with the ERA5 reanalysis, a bilinear interpolation scheme is used to interpolate the data from the native grid to the regular 2.5° longitude–latitude grid.

2.3 Morlet wavelet analysis

The Morlet wavelet is generally used for time–frequency analyses to detect localized variations of power within a time series. Here, we apply the Morlet wavelet to the mean Z500 within the latitudinal belt of 50°–70° N to investigate zonal wavelengths. The wavelet transform is given by (Torrence and Compo 1998)

$$W_{\psi}(a,b) = \pi^{-1/2} \int f(j)\psi\left(\frac{j-b}{a}\right)dj, \tag{1}$$

where the term $\psi(j) = \pi^{-1/4}e^{i6j}e^{-j^2/2}$ is the wavelet function, a is the scale, b is the longitudinal position, and $f(j)$ is a longitude-series Z500. Since the wavelet analysis reflects regional wavenumbers, we use the wavelength to depict the wave structure. Considering the 2.5° equally spaced data, the wavelength for each scale is derived by multiplying the scale by the grid length and its corresponding series is the real part of the wavelet transform. The wavelet power spectrum is defined as $\left|W_{\psi}(a,b)\right|^2$ and the significance is evaluated based on the sum of the power spectrum over a particular latitude using a red-noise process with lag(-1) autoregression. Given that a longitude-series Z500 is cyclic, the cone of influence for all scales is negligible.

2.4 Planetary waves

We apply spherical harmonic analysis to the daily Z500 to isolate the daily planetary waves of the Northern Hemisphere in a slight adaptation of the method in Xie et al. (2017). The spherical harmonic expansion of Z500 considers both the zonal and meridional wavenumbers simultaneously, and is defined as

$$Z500 = \sum_{m=0}^{M} \sum_{n=m}^{N} \left[Z500_n^m P_n^m(\sin\varphi)e^{im\lambda}\right], \tag{2}$$

where λ is longitude, φ is latitude, and $P_n^m(\sin\varphi)$ are the normalized associated Legendre functions:

$$P_n^m(\sin\varphi) = \left[\frac{(2n+1)(n-m)}{2(n+m)!}\right]^{1/2} \left[\frac{\left(1-\sin^2\varphi\right)^{m/2}}{2^n n!}\right] \times \left[\frac{d^{(m+n)}}{d\sin^{(m+n)}\varphi}\left(\sin^2\varphi - 1\right)^n\right]. \tag{3}$$

Since the data are on a 2.5° longitude–latitude grid, M and N are 72. To focus on the Northern Hemisphere, a symmetrical distribution of the daily Z500 about the equator is assumed to calculate the coefficients. Unlike Xie et al. (2017) in which a triangular truncation was used, we adopt an analogue rhomboid truncation with ($m = 5$, $n = m + 6$), in which zonal wavenumbers (m) no more than 5 and meridional wavenumbers ($\frac{n-m}{2}$) no more than 3 are retained (Table 1). In addition, we remove the total wavenumber 0 (i.e. $m = 0$, $n = 0$), which represents the areal mean of Z500 over the Northern Hemisphere. By removing this component, the planetary waves are more comparable in different time periods.

2.5 Clustering planetary waves

In comparison with K-means and hierarchical clustering, an SOM groups high-dimensional data into a small number of SOM patterns in a geometrical similarity neurons structure (Kohonen 2001). The truncated daily Z500 of 4752 grid points over (0°–357.5° E, 10°–90° N) are converted to a row vector for 2196 days (61 days × 36 years). The 2196 row vectors are input into a batch SOM to obtain the SOM patterns by implementing the SOM toolbox version 2.0 (http://www.cis.hut.fi/projects/somtoolbox/about). Initially, a number of random nodes/neurons are specified with a weight vector and a position in the two-dimensional grid, and are then updated by averaging the data samples in the neighborhood of the ''best matching unit'' in each training step. The output is

an SOM with a prescribed number of nodes that represent cluster-mean spatial patterns (i.e., best matching units) of the input truncated daily Z500. The optimum number of SOM patterns should be large enough to accurately capture the planetary wave patterns but small enough to sufficiently differ from each other. To determine the optimum number of SOM nodes, the SOM is repeated with the grid numbers from 1 × 2 to 1 × 20. We calculate average pattern correlations between each row vector of truncated daily Z500 and their corresponding centroids (Lee and Feldstein 2013) and the mean distance between each cluster pair in a slight adaptation of Ward's distance (Ward 1963; Lee et al. 2017).

The SOM clustering indices are determined by finding the "best matching units" to the truncated daily Z500. These indices are used to composite the truncated daily Z500 to construct the planetary wave patterns, which are analogues of the time mean.

3 Planetary wave features

3.1 Intraseasonal transition of planetary waves

Figure 2 displays the climatological mean Z500 and eddies in May and June and their differences. The planetary wave structure in May is primarily characterized by a wavenumber 2 with ridges over western North America and Europe and troughs over eastern Asia to the North Pacific and northeastern North America (Fig. 2a). The ridge and trough pair over the Eastern Hemisphere is broader than that over the Western

Table 1 The zonal and meridional wavenumbers for the truncation of spherical harmonic analysis

	Meridional wavenumber					
Zonal wavenumber	(0, 0)					
		(1, 0)				
	(0, 1)		(2, 0)			
		(1, 1)		(3, 0)		
	(0, 2)		(2, 1)		(4, 0)	
		(1, 2)		(3, 1)		(5, 0)
	(0, 3)		(2, 2)		(4, 1)	
		(1, 3)		(3, 2)		(5, 1)
			(2, 3)		(4, 2)	
				(3, 3)		(5, 2)
					(4, 3)	
						(5, 3)

Fig. 2 Climatological mean Z500 (contours; unit: gpm) and the corresponding latitudinal deviation field (shading) in **a** May and **b** June, as well as **c** the difference between June and May. The contours are drawn every 50 and thin lines indicate zero. The lowest point in each panel is drawn at (90° E, 10° N)
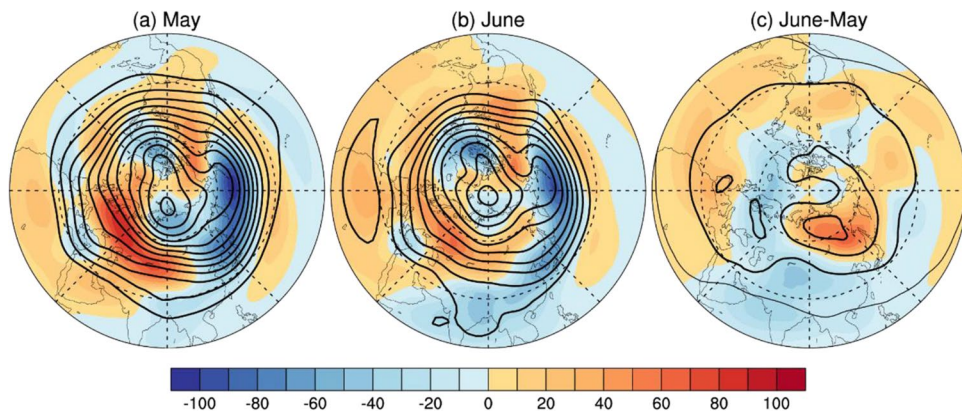

Hemisphere. The polar vortex is meridionally elongated with a center over the Taymyr Peninsula. Although the mid- and high-latitude planetary wave structure in June resembles that in May, the polar vortex displaces northward and a moderate ridge appears over northeastern Asia (Fig. 2b), which is the strongest change between June and May (Fig. 2c). Meanwhile, the circumpolar contours have drifted poleward and are confined to the north to 30° N. In the subtropical region, a closed high over northern Africa is more pronounced and a trough over the Bay of Bengal is further deepened. Since the Sverdrup regime and Rossby regime are separated by the jet stream (Chen 2005), we limit our attention to the planetary waves over mid and high latitudes.

Given that the most prominent change is over northeastern Asia, we average the Z500 within the latitudinal belt of 50°–70° N, which encompasses this largest positive Z500 anomaly. Since the mean Z500 of the latitudinal belt of 50°–70° N does not include the latitudinal shear, we investigate the planetary wave feature in term of eddies relative to the zonal mean. Figure 3 displays a Hovmöller diagram of the climatological mean Z500 eddies averaged between 50° N and 70° N. Inspection of Fig. 3 shows that

Fig. 3 Hovmöller diagram of the Z500 latitudinal deviation field (unit: gpm) averaged within the latitudinal belt of 50°–70° N. The top panel shows the topographic features over 50°–70° N
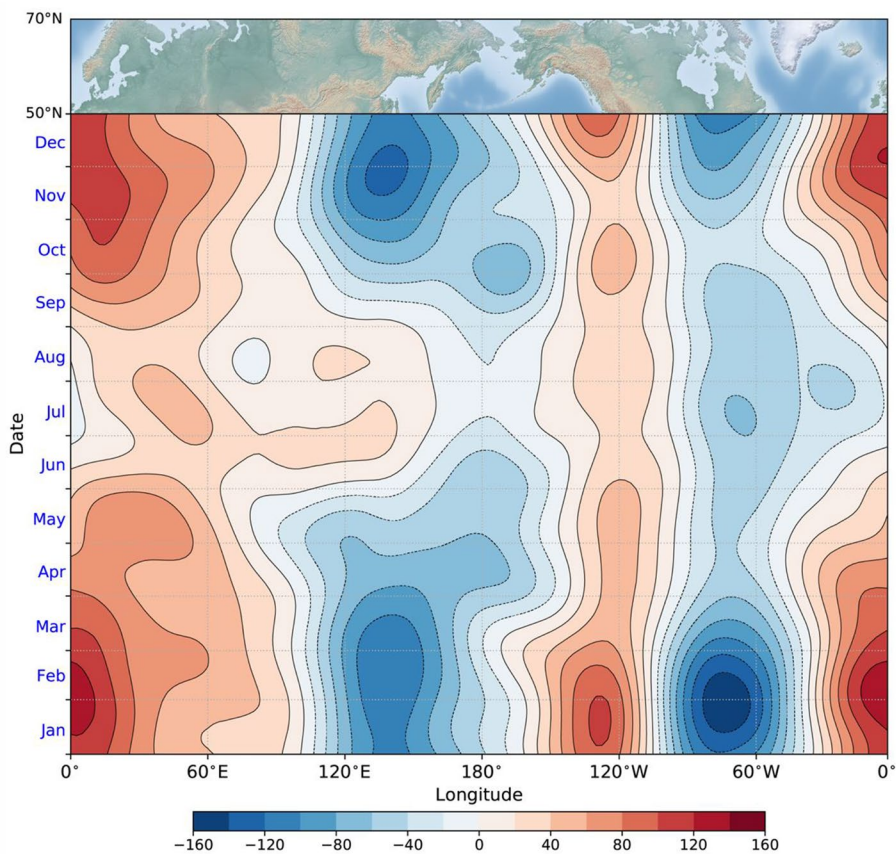
the annual cycle of planetary waves consists of two major periods: the boreal summer (June–August) and winter (November–March) seasons, which are separated by two transitional periods. The planetary waves are primarily characterized by wavenumber 2, with the largest amplitudes in winter and the smallest amplitude in summer. Aside from the change in wave amplitude, the planetary wave phase displaces eastward in summer with respect to winter. The planetary waves weaken from April and turn to be a typical summer pattern in June, with a moderate positive anomaly dominating over the Eurasian continent and a trough confined to the Bering Sea. In contrast, the ridge over western North America exhibits stationary with weaker amplitude and the trough over eastern North America extends to the North Atlantic.

As noted above, the planetary waves exhibit different spatial features over the Northern Hemisphere, we adopt Morlet wavelet analysis to decompose the planetary waves into different wavelengths and corresponding power spectra. Figure 4 shows the real coefficients and power spectra of planetary waves in May and June, respectively. The planetary waves in May are dominantly contributed by wavelengths of around 10,000 km, which corresponds to zonal wavenumber 2 (Fig. 4a). In contrast, the overall power spectrum of planetary waves in June exhibits
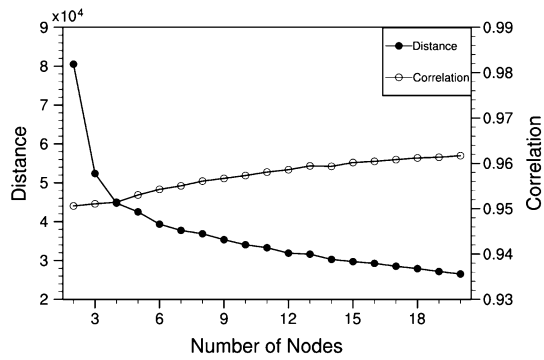
a bimodal pattern with new significant wavelengths of around 7000 km (Fig. 4b), which corresponds to wavenumber 3. The wavelengths of around 10,000 km in June not only drastically weaken in amplitude but also displace slightly eastward with respect to May, while the wavelengths of around 7000 km amplify and shift slightly westward. The wavelengths of around 7000 km are stronger and in-phase with the wavelengths of around 10,000 km in the Western Hemisphere, whereas they are out-of-phase with the wavelengths of around 10,000 km in the Eastern Hemisphere. Therefore, the planetary waves exhibit a drastic change in the Eastern Hemisphere, particularly over northeastern Asia, where the positive height anomaly of wavelengths of around 7000 km is superior to the negative height anomaly of wavelengths of around 10,000 km.

3.2 Cluster-mean planetary wave patterns

As mentioned in the introduction, planetary waves can also be obtained from the daily Z500 using spatiotemporal spectral analysis (Hayashi 1977; Watt-Meyer and Kushner 2015). The planetary wave variability discussed above is based on the monthly mean, but, to a certain extent, such a time period is somewhat subjective. In this section, we apply the SOM, which outputs consecutive spatial patterns, to daily

Fig. 4 Wavelet power spectra (shading) and real coefficient (contours; unit: gpm) of the average Z500 within the latitudinal belt of 50°–70° N during **a** May and **b** June. The global wavelet power spectra (blue line) with the 95% confidence level (dashed red line) using the corresponding red-noise spectra are shown to the right

truncated Z500 to construct the planetary wave patterns based on the cluster mean. Since we focus on the planetary-scale structures, daily synoptic waves are discarded before the SOM is produced to remove their potential influence on the clustering.
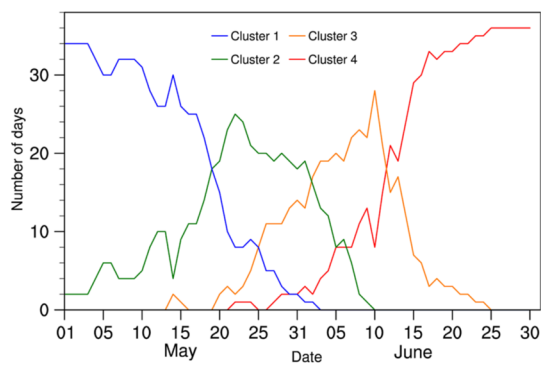
3.2.1 Planetary wave clustering

As introduced in Sect. 2.5, the SOM is repeatedly generated with grid numbers varying from 1×2 to 1×20 to determine the optimum separation of planetary wave patterns. Figure 5 displays the mean correlation coefficient between the daily truncated Z500 and the corresponding cluster centroid, as well as the mean distance between each pair of cluster centroids. The distance increases smoothly from 1×20 to 1×4, and then drastically to 1×3 and 1×2, suggesting that the four clusters differ considerably from each other and cannot be merged further. In contrast, the change in correlation coefficient is relatively smooth. According to the distance measure, we consider the 1×4 SOM grid as the optimum cluster number. Since we try to isolate planetary wave patterns varying in one direction (i.e. from 1 May to 30 June), we prefer the 1×4 SOM grid to the 2×2 grid, in which all SOM patterns are connected with each other.

3.2.2 Planetary wave patterns

Figures 6 and 7 display the composite truncated daily Z500 and anomalies relative to the climatological mean of May and June and the intraseasonal time series of occurrence number for the four planetary wave patterns, respectively. Wavenumbers 1–5 of the climatological mean circulations consist with the unfiltered climatological mean flows but with smoother contours (Figs. 2a, b, 6a, b). The four planetary wave patterns vary progressively from the structure resembling the climatological mean flow of May to June. The anomalous fields relative to the climatological
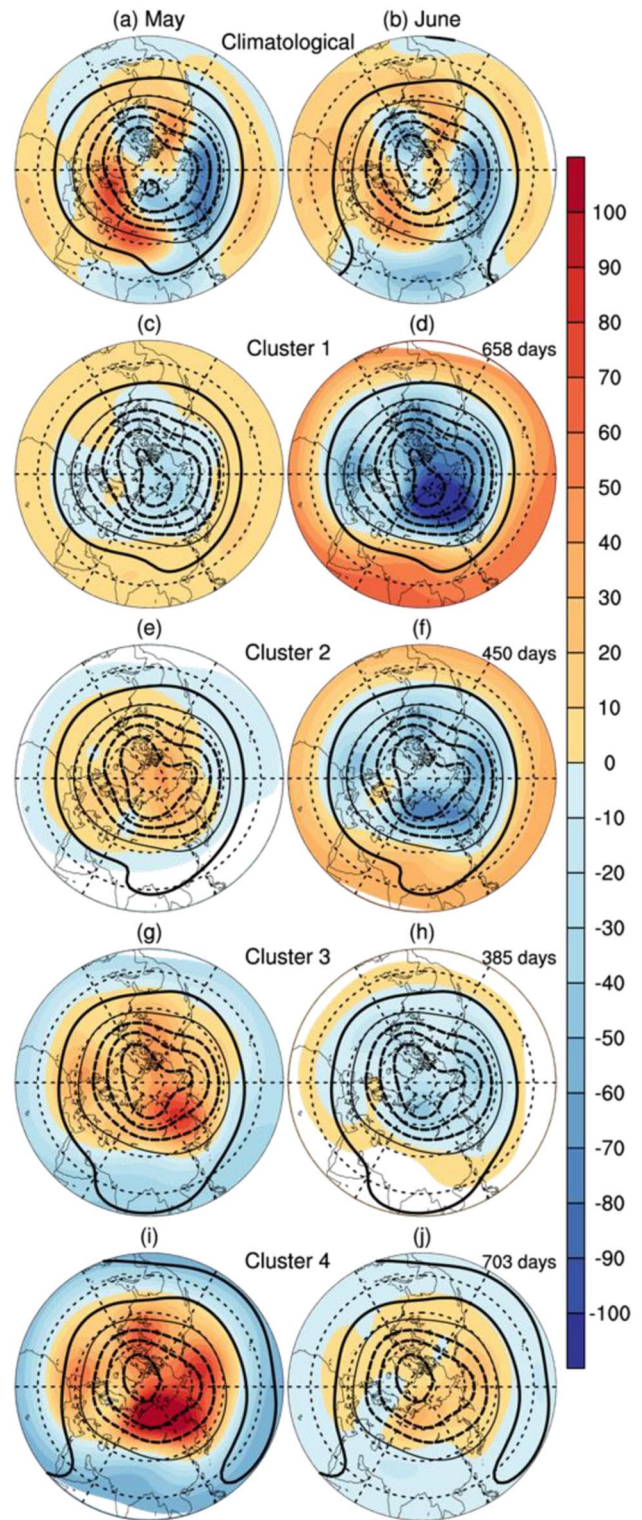
Fig. 6 Climatological mean daily truncated Z500 (contours; unit: gpm) and the corresponding latitudinal deviation field (shadings) in **a** May and **b** June. Composite daily truncated Z500 (contours) and corresponding anomalies relative to climatological mean in May (left column) and June (right column) for cluster 1 (**c, d**), cluster 2 (**e, f**), cluster 3 (**g, h**) and cluster 4 (**i, j**) of planetary waves. The contours are drawn every 50 and thin lines indicate zero. The lowest point in each panel is drawn at (90° E, 10° N)

Fig. 7 Time series of the occurrence number of four planetary wave clusters

mean feature a positive phase of the Northern Annular Mode (NAM) to a negative phase of the NAM. The occurrence number of the four planetary wave patterns peaks in sequence (Fig. 7).

The first planetary wave pattern is characterized by a positive phase of the NAM, suggesting a deepened polar vortex and stationary troughs (Fig. 6c, d). The polar vortex slides toward the Taymyr Peninsula. This pattern primarily occurs in the leading three weeks of May and then declines drastically to zero in early June (Fig. 7). The second and third planetary wave patterns are intermediate patterns between the climatological mean flows in May and June, and their anomalies exhibit a negative NAM and a positive NAM relative to May and June, respectively (Fig. 6e–h). Such anomalous circulation indicates amplifications of stationary ridges and attenuations of stationary troughs and the polar vortex. The polar vortex exhibits a fanning structure from Greenland to the Taymyr Peninsula. Considering the second pattern (Fig. 6e, f), the ridge over western North America extends northward to the Arctic Ocean. This pattern mainly occurs over the period from mid-May to early June (Fig. 7). In comparison, a new moderate ridge is seen over northeastern Asia, with the most prominent positive anomaly change with respect to planetary waves in May for the third planetary wave pattern (Fig. 6g, h), which takes place from late May to mid-June (Fig. 7). Considering the fourth planetary wave pattern (Fig. 6i, j), the anomalies relative to the planetary waves in May and June both resemble a negative phase of the NAM. The polar vortex is reduced in size to Greenland, suggesting amplifications of ridges over northeastern Asia and western North America. This fourth pattern occurs in roughly the last three weeks of June (Fig. 7).

To test the sensitivity of our results to the clustering method employed, we apply the K-means method to the daily truncated Z500 fields with $K = 4$ (i.e., the same input data used in creating the SOM clustering results). The spatial patterns derived using the K-means approach closely resemble those obtained from the SOM clustering, in which the spatial

pattern correlation coefficients are 0.998, 0.997, 0.994 and 0.998, respectively. Unlike the SOM clustering result, the planetary wave patterns obtained from the K-mean method exhibit more overlaps in their occurrence dates. For example, the number of days associated with the second planetary wave pattern is relatively high (around 10 days) in the first week and reaches one of maxima with 20 days in the second week of June (Figure not shown).

In comparison with prior studies that considered planetary waves as the monthly or seasonal mean, the planetary waves in this study include the latitudinal shear of the zonal mean. The planetary wave patterns identified here exhibit pronounced intraseasonal variabilities in both amplitude and spatial structure. This is also in contrast with the daily planetary wave isolated by spatiotemporal spectral analysis, which primarily fluctuates in the amplitude of the planetary waves.

To calculate time scales of the four planetary wave patterns, we first construct daily planetary wave pattern indices by projecting each daily Z500 (Z_{daily}) on planetary wave patterns ($Z_{planetary}$) using a pattern amplitude projection (Deng et al. 2012):

$$\text{Planetary wave pattern index} = \frac{A^{-1} \int_A a^2 Z_{daily} Z_{planetary} \cos \phi \, d\lambda \, d\phi}{A^{-1} \int_A a^2 \left(Z_{planetary}\right)^2 \cos \phi \, d\lambda \, d\phi} \tag{4}$$

where A represents the area over (10°–90° N, 0°–360° E), a is the mean radius of the Earth, and λ and ϕ are the longitude and latitude, respectively. Then, we apply the e-folding time scale procedure provided by Gerber et al. (2008) to the time series of daily indices of each planetary wave pattern. The result shows that the four planetary wave patterns have time scales of 7.7–14.1, 7.3–11.2, 7.7–18.2 and 7.5–12.9 days, respectively. The time scale analysis of planetary wave patterns illustrates that variability of planetary wave is intraseasonal in nature.

We again apply Morlet wavelet analysis to the Z500 averaged within the latitudinal belt of 50°–70° N to examine each phase and amplitude of different wavenumbers for the four planetary wave patterns. Figure 8 displays the real coefficients and power spectra for the four planetary wave patterns. The overall impression from Figs. 4 and 8 is one of similarity in wavelengths of around 10,000 km, which weaken gradually and displace eastward. However, there is an interesting difference in the wavelengths of around 7000 km in that they intensify first and then weaken in amplitude. Wavelengths of around 10,000 km dominate in the first pattern and decline roughly by half in amplitude for the second pattern, while the amplitude of wavelengths of around 7000 km increases and turns to be significant at the 95% confidence level (Fig. 8a, b). Although the second pattern is predominated by wavelengths of around 10,000 km, the wavelengths of around 7000 km are out-of-phase with

Fig. 8 As in Fig. 4 but for **a** cluster 1, **b** cluster 2, **c** cluster 3 and **d** cluster 4 of planetary waves
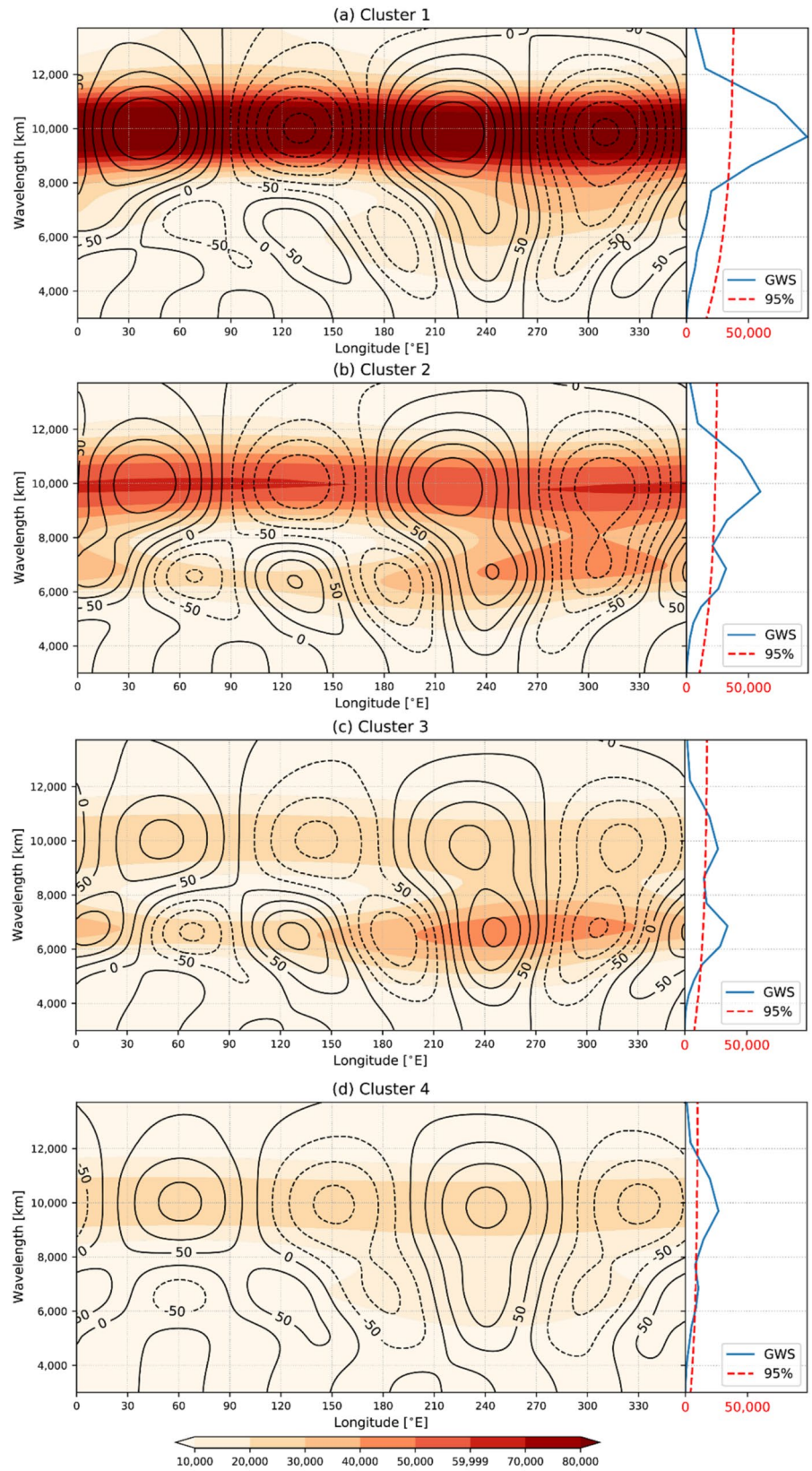
the wavelengths of around 10,000 km over the Eastern Hemisphere and thus weaken the negative anomaly of the planetary waves over northeastern Asia.

Considering the third pattern (Fig. 8c), wavelengths of around 10,000 km decline further by more than half in terms of amplitude and displace slightly eastward in comparison with the second pattern. In contrast, wavelengths of around 7000 km magnify in amplitude and regress westward. The amplitude of the wavelengths of around 7000 km exceeds that of the wavelengths of around 10,000 km over northeastern Asia (90°–150° E), rendering a positive anomaly over that region. Unlike the second and third patterns, the amplitudes of the wavelengths of around 10,000 km and 7000 km both decrease in the fourth pattern (Fig. 8d). Waves of wavelengths of around 10,000 km displace further eastward by about 10° and those of around 7000 km shift westward, in which they are in-phase with each other at around 240° E but out-of-phase at around 60° E. Wavelengths of around 7000 km show a positive center over northeastern Asia and overlap with a node of wavelengths of around 10,000 km, delivering a positive anomaly of the stationary eddy in-situ. In comparison with monthly mean planetary waves, the cluster-mean planetary waves reveal that the planetary waves exhibit rather different characteristics in June.

4 Planetary wave response to Asian mountain forcing

Prior studies have shown an evident circulation response over northeastern Asia to the Tibetan Plateau forcing (Ting et al. 2001; Held et al. 2002; Chang 2009). The nonlinearity, which represents nonlinear wave–wave interactions among the waves forced by orography, diabatic heating and transient eddies, generates opposite circulations around Lake Baikal during winter and summer (Ting et al. 2001). Such circulations are substantially contributed by the nonlinear wave-wave interaction between the flows forced by the orography and diabatic heating. In light of these findings, we use GMMIP Tier-3 experiments from a sophisticated model that not only considers the sensible heating distribution associated with the mountains over Asia (above 500 m), but also nonlinear wave-wave interactions between the flows forced by the orography and sensible heating (He et al. 2019a, 2020). Following Held et al. (2002), we refer to AMIP as the total forcing that produce the simulation $F(AMIP)$ and $F(AMIP)−F(TIP)$ as the full nonlinear forcing response to the Asian mountains denoted by TIP. The full nonlinear forcing to sensible heating and dynamical forcings associated with the mountains of Asia are $F(SH)=F(AMIP)−F(TIP\_nosh)$ and $F(DYN)=F(TIP\_nosh)−F(TIP)$, respectively.

Figure 9 displays the monthly mean truncated Z500 for the AMIP and full nonlinear responses to the mountains of Asia. The simulated climatological mean Z500 in May and June generally agree with the reanalysis over the mid and high latitudes (Figs. 2, 6a, b, 9a–c). The model successfully reproduces the largest positive Z500 anomaly over northeastern Asia but with a stronger amplitude and a larger southeastward extension (Fig. 9c). Meanwhile, the model also yields larger positive Z500 anomalies over the North Pacific, the Great Lakes and Great Britain. In terms of the full nonlinear response to the mountains of Asia, it mainly amplifies the climatological planetary waves, particularly over the Eastern Hemisphere (Fig. 9d–f), which agrees with prior studies (Held et al. 2002; Chang 2009). The ridge from Scandinavia to Lake Baikal magnifies and then extends northeastward to northeastern Asia, resulting in a moderate positive Z500 anomaly there.

The full nonlinear response to the mountains of Asia is then decomposed to full nonlinear responses to sensible heating and dynamical forcings associated with the mountains of Asia, respectively (Fig. 9g–l). The noticeable feature of this decomposition is the offset over East Asia and the North Pacific between full nonlinear responses to sensible heating and dynamical forcings associated with the mountains of Asia, suggesting a major contribution of sensible heating forcing associated with the mountains of Asia to the largest Z500 anomaly over northeastern Asia. More specifically, the full nonlinear response to the sensible heating forcing associated with the mountains of Asia is characterized by positive Z500 anomalies over the mid and high latitudes and negative Z500 anomalies over the subtropical region (Fig. 9g, h). A conspicuous positive Z500 anomaly center elongates from the Tibetan Plateau to the Northeast Pacific in May and withdraws toward northeastern Asia in June, delivering the largest positive Z500 anomaly over northeastern Asia (Fig. 9g–i). In contrast, although the full nonlinear response to dynamic forcing associated with the mountains of Asia resembles that to the mountains of Asia, it features a negative Z500 anomaly over East Asia to the North Pacific in both May and June (Fig. 9j–l). Therefore, the dynamical forcing associated with the mountains of Asia exhibits a detrimental influence on the formation and maintenance of the warm ridge over northeastern Asia.
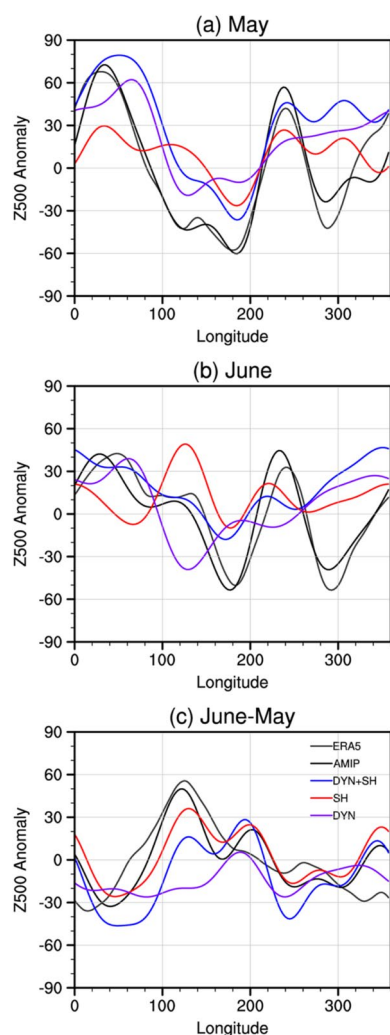
To focus on the largest positive Z500 anomaly over northeastern Asia, Fig. 10 displays the deviation of Z500 averaged within the latitudinal belt of 50°–70° N from the zonal mean for the ERA5 reanalysis, the AMIP simulation and GMMIP experiments. The planetary wave eddies of the AMIP simulation are in good agreement with those of ERA5, which are a wave of roughly wavenumber 2. The AMIP simulation has a positive bias around Great Britain in May, where the full nonlinear responses to the mountains of Asia all tend to yield positive Z500 anomalies. Considering this deficiency of the model, we narrow down our discussion to the region over 0°–270° E.

Fig. 9 Climatological mean Z500 (contours; unit: gpm) and the corresponding latitudinal deviation field (shading) in **a** May and **b** June, as well as **c** the difference between June and May for the AMIP simulation. The full nonlinear responses in Z500 to (**d–f**) the mountains of Asia, **g–i** sensible heating forcing associated with the mountains of Asia, and **j–l** dynamical forcing associated with the mountains of Asia. The left, middle and right columns refer to May, June and the difference between June and May, respectively. The contours are drawn every 50 and thin lines indicate zero. The lowest point in each panel is drawn at (90° E, 10° N)
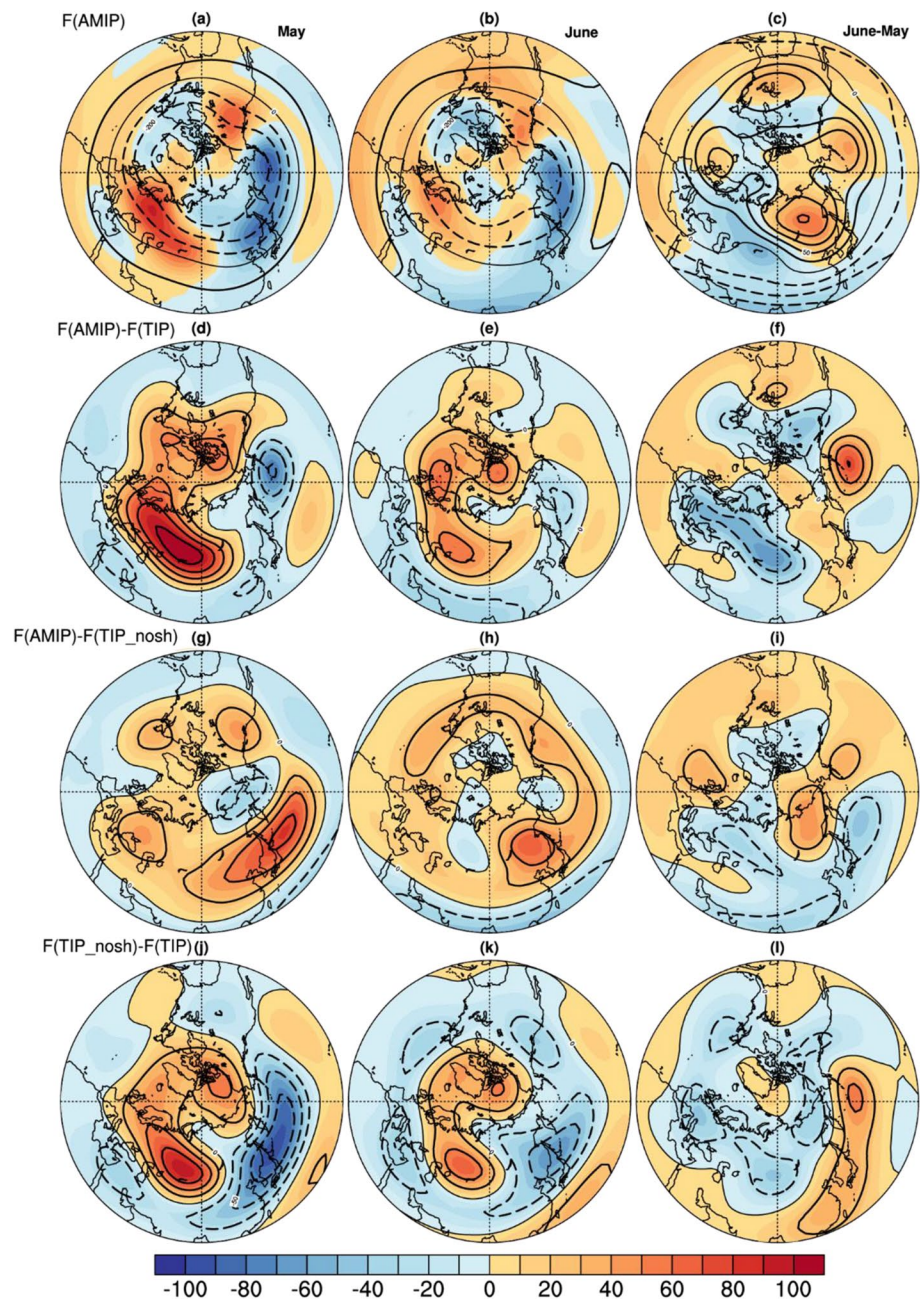
The full nonlinear response to the mountains of Asia in May provides a pronounced contribution to two ridges over Europe and North America and a moderate contribution to the trough from East Asia to the North Pacific (Fig. 10a). The contribution to the ridge is mainly from the full nonlinear response to dynamical forcing associated with the mountains of Asia. In contrast, the full nonlinear response to sensible heating associated with the mountains of Asia deepens the trough over the North Pacific and yet offsets the trough over northeastern Asia. In June (Fig. 10b), the full nonlinear response to the mountains of Asia exhibits a sizeable contribution to the planetary waves over Eurasia and a moderate contribution to the planetary waves over the North Pacific and North America. Although there is more offsetting between the full nonlinear responses to sensible heating and dynamical forcings associated with the mountains of Asia over northeastern Asia, the full nonlinear response to sensible heating forcing associated with the mountains of Asia is superior to its dynamical forcing counterpart. Therefore, a discernible stationary ridge rides over northeastern Asia. The contribution of the full nonlinear response to sensible heating forcing associated with the mountains of Asia also plays

Fig. 10 Deviation of Z500 averaged within the latitudinal belt of 50°–70° N from the zonal average during **a** May and **b** June in ERA5 (gray), AMIP (black), the full nonlinear response to the mountains of Asia (blue), and the full nonlinear responses to sensible heating (red) and dynamical forcings (purple) associated with the mountains of Asia. **c** is the difference between (**b**) and (**a**)

a dominant role in the largest positive Z500 anomaly in planetary waves over northeastern Asia (Fig. 10c).

The results in Sect. 3 showed that the planetary waves can be separated into four patterns on the intraseasonal time scale from May to June, and the largest positive Z500 anomaly over northeastern Asia appears first in the third planetary wave pattern. It is of interest to examine the intraseasonal variability of the planetary waves associated with the forcings of the mountains of Asia. Since the full nonlinear responses to each forcing are derived in terms of anomalies, it is hard to determine their corresponding planetary wave clusters. As an alternative, we construct a planetary wave pattern index by projecting each daily truncated Z500 (Z_{daily}) of F(AMIP), F(TIP) and F(TIP_nosh)

on each planetary wave pattern ($Z_{stationary}$) using Eq. 4. Figure 11 displays the probability density functions (PDFs) of planetary wave pattern indices for the AMIP simulation, and the full nonlinear responses to the mountains of Asia [F(AMIP) – F(TIP)], sensible heating forcing associated with the mountains of Asia [F(AMIP)-F(TIP_nosh)], as well as dynamical forcing associated with the mountains of Asia [F(TIP_nosh) – F(TIP)]. The PDFs of the AMIP simulation are generally above 0.9, indicating good performance of the model in simulating the intraseasonal planetary wave patterns.

In terms of the first and second planetary wave patterns (Fig. 11a, b), the mountain forcing tends to produce more index values that are relatively larger and fewer that are relatively smaller. Such a distribution is mainly contributed by the full nonlinear response to dynamical forcing associated with the mountains of Asia, indicating that dynamical forcing likely produces the first and second planetary wave patterns. In contrast, the full nonlinear response to sensible heating forcing associated with the mountains of Asia increases the amount of larger index values for the third and fourth planetary wave patterns (Fig. 11c, d). Despite the more index values that are larger for the fourth planetary wave pattern induced by sensible heating forcing associated with the mountains of Asia, it is offset to a greater extent by dynamical forcing associated with the mountains of Asia. Therefore, the full nonlinear response to the mountains of Asia tends to result more in the generation of the third planetary wave pattern and thus induces the largest positive Z500 anomaly over northeastern Asia. This is also inferred when comparing Figs. 6 and 9, in that the response to the sensible heating forcing associated with the mountains of Asia is a positive anomaly over the mid and high latitudes, mimicking the fourth planetary wave pattern. However, the response to dynamical forcing associated with the mountains of Asia offsets that to the sensible heating forcing associated with the mountains of Asia, particularly from East Asia to the North Pacific. Therefore, the full nonlinear response to the mountains of Asia tends to produce the third planetary wave pattern more than the fourth planetary wave pattern.

5 Summary and discussion

In this study, we have examined the intraseasonal transition of planetary waves in terms of Z500 over the Northern Hemisphere during May and June, when the so-called abrupt change of planetary waves takes place. Unlike prior studies in which the zonal mean was removed to define the planetary waves, the planetary waves considered here include the latitudinal shear of the zonal mean. The abrupt change of planetary waves is characterized by the largest positive

Fig. 11 The PDFs of projection indices of planetary wave patterns for **a** cluster 1, **b** cluster 2, **c** cluster 3 and **d** cluster 4 in AMIP (gray). The anomalous PDFs of projection indices of planetary wave patterns for the full nonlinear response to the mountains of Asia (blue), and the sensible heating (red) and dynamical forcings (purple) associated with the mountains of Asia
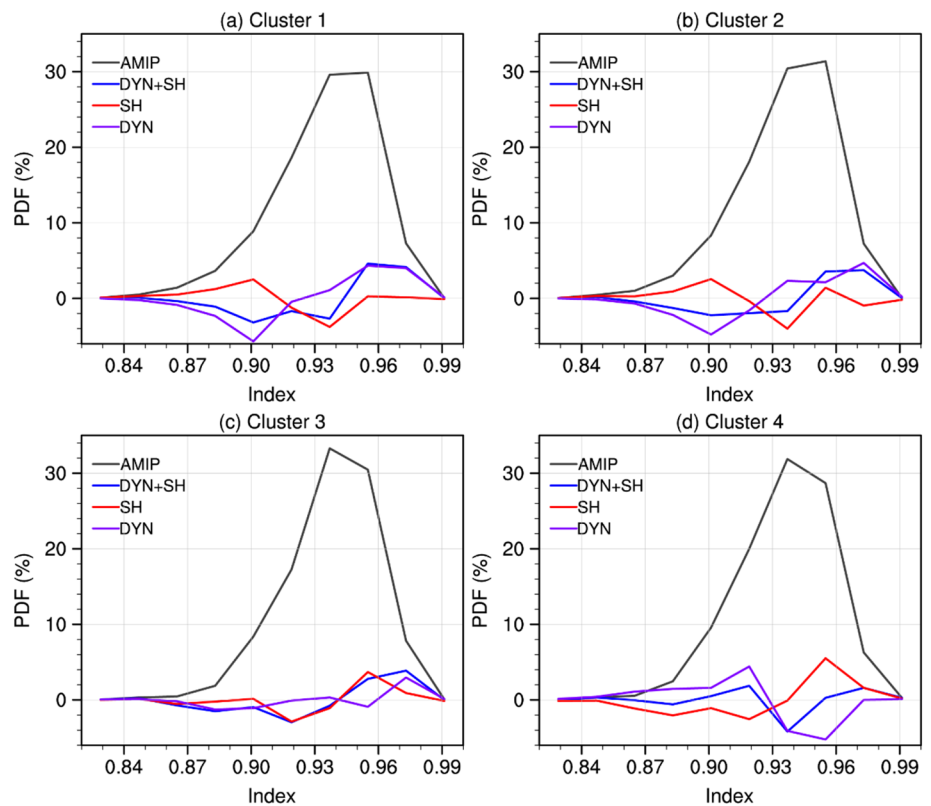
Z500 anomaly over northeastern Asia. Morlet wavelet analysis was applied to the Z500 averaged within the latitudinal belt of 50°–70° N, which encompasses the largest positive Z500 anomaly over northeastern Asia, to assess the relative contribution of each wavelength to the intraseasonal change in planetary waves. The intraseasonal change in planetary waves is further discussed based on the cluster mean derived by applying an SOM to the daily truncated Z500 of wavenumbers 1–5. Orographic perturbation experiments from GMMIP were adopted to investigate the relative contributions to the largest positive Z500 anomaly over northeastern Asia from the full nonlinear response to the forcing by the mountains of Asia.

The largest positive Z500 anomaly over northeastern Asia during the period from May to June results from the interaction between wavelengths of around 10,000 km and 7000 km, which correspond to zonal wavenumbers 2 and 3, respectively. Although the monthly mean planetary waves provide an overview of the intraseasonal variability of each wavenumber belt, the time period in deriving the planetary waves is somewhat subjective. The SOM applied to the daily truncated Z500 identifies four planetary wave patterns that occur in sequence from May to June. The anomalous fields relative to the climatological mean feature a positive phase of the NAM to a negative phase of the NAM. Meanwhile, a positive change over northeastern Asia amplifies gradually from the second to the fourth

planetary wave pattern. Considering the planetary waves averaged within the latitudinal belt of 50°–70° N, wavelengths of around 10,000 km and 7000 km are in- and out-of-phase with each other over the Western Hemisphere and Eastern Hemisphere, respectively. Therefore, the planetary waves maintain the phase over the Western Hemisphere during May and June. Wavelengths of around 10,000 km weaken in amplitude and displace eastward, while those of around 7000 km magnify gradually from the first to third pattern and weaken in the fourth pattern. Therefore, the largest positive Z500 anomaly over northeastern Asia is primarily contributed by wavelengths of around 7000 km and the third planetary wave pattern.

The full nonlinear response to the forcing by the mountains of Asia, particularly that associated with sensible heating forcing associated with the mountains of Asia, provides a considerable contribution to the largest positive Z500 anomaly over northeastern Asia. The full nonlinear response to the Asian mountains forcing acts to intensify the stationary ridge and trough over the Eastern Hemisphere. The full nonlinear responses to sensible heating and dynamical forcings associated with the mountains of Asia offset each other over East Asia. The positive anomaly response to sensible heating forcing associated with the mountains of Asia over northeastern Asia enhances from May to June, while the negative height anomaly response to dynamical forcing associated with the mountains of Asia over northeastern Asia weakens.

Consequently, the full nonlinear response to the combination of sensible heating and dynamical forcings associated with the mountains of Asia contributes to the largest positive Z500 anomaly over northeastern Asia. The full nonlinear response to dynamical forcing associated with the mountains of Asia in Z500 is mainly wavenumber 2 and thus overproduces the first and second planetary wave patterns. In contrast, the full nonlinear response to sensible heating forcing associated with the mountains of Asia is characterized by positive anomalies over the mid and high latitudes, which is more likely to produce the third and fourth planetary wave patterns. Given the offsetting responses over northeastern Asia between sensible heating and dynamical forcings associated with the mountains of Asia, the full nonlinear response to the mountains of Asia overproduces the third planetary wave pattern rather than the fourth planetary wave pattern.

In terms of the transient eddy feedback forcing, we speculate that its contribution to planetary waves mimics that of the dynamical forcing associated with the mountains of Asia. The response to the transient eddy feedback forcing is generally characterized by two major dipoles, with negative anomalies poleward to positive anomalies over the North Pacific and the North Atlantic (Held et al. 2002). Chang (2009) demonstrated that the orographic forcing of the Tibetan Plateau substantially suppresses the activity of transient eddies over the continents. Therefore, the response to transient eddy feedback forcing over East Asia bears some resemblance with that to the dynamical forcing of the mountains of Asia, which offsets the positive Z500 anomaly over northeastern Asia. From May to June, the response to the transient eddy feedback forcing weakens and thus the offsetting of the positive Z500 anomaly over northeastern Asia reduces.

It has been noted by Chyi et al. (2021) that the formation of a warm anticyclone anomaly over northeastern Asia in early June is associated with snowmelt in Eurasia. We acknowledge a potential positive contribution from snowmelt to the largest Z500 anomaly over northeastern Asia. The snowmelt over northern Asia increases the water vapor in the atmosphere by receiving more solar heating in June. The upward motion of water vapor condenses in the troposphere and thereby releases latent heat to the atmosphere, which could provide a discernible positive contribution to the warm ridge over northeastern Asia.

Prior studies regarding the transition of the seasons have primarily focused on the onset of the East Asian monsoon. In contrast, we limited our attention to investigating the largest positive Z500 anomaly over northeastern Asia. It has been well established that such a positive Z500 anomaly over northeastern Asia exports Rossby wave energy southward in the mid and high troposphere and induces the Northeast China cold vortex or the well-known Mei-yu trough (e.g.

Bueh et al. 2008). This study simply uses the orographic perturbation experiment from GMMIP; more suitable experiments will be conducted in future work.

References

Bueh C, Shi N, Ji L, Wei J, Tao S (2008) Features of the EAP events on the medium-range evolution process and the mid- and high-latitude Rossby wave activities during the Meiyu period. Chin Sci Bull 53:610–623. https://doi.org/10.1007/s11434-008-0005-2

Chang EKM (2009) Diabatic and orographic forcing of northern winter stationary waves and storm tracks. J Clim 22(3):670–688. https://doi.org/10.1175/2008JCLI2403.1

Charney JG (1947) The dynamics of long waves in a baroclinic westerly current. J Meteorol 4:135–162. https://doi.org/10.1175/1520-0469(1947)004%3c0136:TDOLWI%3e2.0.CO;2

Charney JG, Eliassen A (1949) A numerical method for predicting the perturbations of the middle latitudes westerlies. Tellus 1:38–54. https://doi.org/10.1111/j.2153-3490.1949.tb01258.x

Chen TC (2005) The structure and maintenance of stationary waves in the winter Northern Hemisphere. J Atmos Sci 62:3637–3660. https://doi.org/10.1175/JAS3566.1

Chen P, Peng J, Bueh C, Gong Y (2021) The connection of the summer onset in Northern Asia with the precipitation anomalies in Eastern China during the Meiyu period. Clim Environ Res. https://doi.org/10.3878/j.issn.1006-9585.2021.21057(inChinese)

Chyi D, Bueh C, Xie Z (2021) Summer onset in northern Asia. Int J Climatol 41:1094–1111. https://doi.org/10.1002/joc.6753

Deng Y, Park TW, Cai M (2012) Process-based decomposition of the global surface temperature response to El Nino in boreal winter. J Atmos Sci 69(5):1706–1712. https://doi.org/10.1175/JAS-D-12-023.1

Eady ET (1949) Long waves and cyclone waves. Tellus 1:33–52. https://doi.org/10.1111/j.2153-3490.1949.tb01265.x

Garfinkel CI, White I, Gerber EP, Jucker M, Erez M (2020) The building blocks of Northern Hemisphere wintertime stationary waves. J Clim 33(13):5611–5633. https://doi.org/10.1175/JCLI-D-19-0181.1

Hayashi Y (1977) On the coherence between progressive and retrogressive waves and a partition of space-time power spectra into standing and traveling parts. J Appl Meteorol 16:368–373. https://doi.org/10.1175/1520-0450(1977)016%3c0368:OTCBPA%3e2.0.CO;2

He B, Bao Q, Wang X et al (2019a) CAS FGOALS-f3-L model datasets for CMIP6 historical Atmospheric Model Intercomparison Project simulation. Adv Atmos Sci 36(8):771–778. https://doi.org/10.1007/s00376-019-9027-8

He B, Liu Y, Wu G et al (2019b) The role of air–sea interactions in regulating the thermal effect of the Tibetan-Iranian Plateau on the

Asian summer monsoon. Clim Dyn 52:4227–4245. https://doi.org/10.1007/s00382-018-4377-y

He B, Liu Y, Wu G et al (2020) CAS FGOALS-f3-L model datasets for CMIP6 GMMIP Tier-1 and Tier-3 experiments. Adv Atmos Sci 37(1):18–28. https://doi.org/10.1007/s00376-019-9085-y

Held IM, Ting M, Wang H (2002) Northern winter stationary waves: theory and modeling. J Clim 15(16):2125–2144. https://doi.org/10.1175/1520-0442(2002)015%3c2125:NWSWTA%3e2.0.CO;2

Hersbach H, Bell B, Berrisford P et al (2020) The ERA5 global reanalysis. Q J R Meteorol Soc 146:1999–2049. https://doi.org/10.1002/qj.3803

Holton JR, Mass C (1976) Stratospheric vacillation cycles. J Atmos Sci 33:2218–2225. https://doi.org/10.1175/1520-0469(1976)033%3c2218:SVC%3e2.0.CO;2

Hoskins BJ, Karoly DJ (1981) The steady linear response of a spherical atmosphere to thermal and orographic forcing. J Atmos Sci 38:1179–1196. https://doi.org/10.1175/1520-0469(1981)038%3c1179:TSLROA%3e2.0.CO;2

Kohonen T (2001) Self-organizing maps, 3rd edn. Springer, Berlin, p 521

Lee S, Feldstein SB (2013) Detecting ozone- and greenhouse gas–driven wind trends with observational data. Science 339:563–567. https://doi.org/10.1126/science.1225154

Lee M, Lee S, Song H, Ho C (2017) The recent increase in the occurrence of a boreal summer teleconnection and its relationship with temperature extremes. J Clim 30(18):7493–7750. https://doi.org/10.1175/JCLI-D-16-0094.1

Li ZJ, Ji LR (1997) Efficient forcing and atmospheric teleconnections. Q J R Meteorol Soc 123:2401–2423. https://doi.org/10.1002/qj.49712354412

Nigam S, DeWeaver E (2015) Stationary waves (orographic and thermally forced), encyclopedia of atmospheric sciences. Second edition, vol 1. Academic Press, London, pp 431–445

Pratt RW, Wallace JM (1976) Zonal propagation characteristics of large–scale fluctuations in the mid–latitude troposphere. J Atmos Sci 33(7):1184–1194. https://doi.org/10.1175/1520-0469(1976)033%3c1184:ZPCOLF%3e2.0.CO;2

Simmons AJ, Wallace JM, Branstator GW (1983) Barotropic wave propagation and instability, and atmospheric teleconnection patterns. J Atmos Sci 40(6):1363–1392. https://doi.org/10.1175/1520-0469(1983)040%3c1363:BWPAIA%3e2.0.CO;2

Sun C, Zhang J, Gong Z, Li J (2019) Meridional structure and characteristic scale of qusi-stationary planetary waves in the Northern Hemisphere. J Beijing Norm Univ (nat Sci) 55(1):1–10 (**in Chinese**)

Tao S, Zhao Y, Chen X (1958) The relationship between May-Yu in Far East and the behavior of circulation over Asia. Acta Meteorol Sin 29(2):119–134 (**in Chinese**)

Ting MF, Held IM (1990) The stationary wave response to a tropical SST anomaly in an idealized GCM. J Atmos Sci 47:2546–2566. https://doi.org/10.1175/1520-0469(1990)047%3c2546:TSWRTA%3e2.0.CO;2

Ting MF, Wang HL, Yu LH (2001) Nonlinear stationary wave maintenance and seasonal cycle in the GFDL R30 GCM. J Atmos Sci 58(16):2331–2354. https://doi.org/10.1175/1520-0469(2001)058%3c2331:NSWMAS%3e2.0.CO;2

Torrence C, Compo GP (1998) A practical guide to wavelet analysis. Bull Am Meteorol Soc 79(1):61–78. https://doi.org/10.1175/1520-0477(1998)079%3c0061:APGTWA%3e2.0.CO;2

Ward JH (1963) Hierarchical grouping to optimize an objective function. J Am Stat Assoc 58:236–244. https://doi.org/10.1080/01621459.1963.10500845

Watt-Meyer O, Kushner PJ (2015) The role of standing waves in driving persistent anomalies of upward wave activity flux. J Clim 28:9941–9954. https://doi.org/10.1175/JCLI-D-15-0317.1

Wu G, Liu Y, Zhang Q, Duan A, Wang T, Wan R, Liu X, Li W, Wang Z, Liang X (2007) The influence of mechanical and thermal forcing by the Tibetan Plateau on Asian climate. J Hydrometeorol 8(4):770–789. https://doi.org/10.1175/JHM609.1

Xie Z, Black RX, Deng Y (2017) Daily-scale planetary wave patterns and the modulation of cold season weather in the northern extratropics. J Geophys Res Atmos 122:8383–8398. https://doi.org/10.1002/2017JD026768

Xie Z, Black RX, Deng Y (2019) Planetary and synoptic-scale dynamic control of extreme cold wave patterns over the United States. Clim Dyn 53:1477–1495. https://doi.org/10.1007/s00382-019-04683-7

Ye D, Tao S, Li M (1958) The abrupt change of atmospheric circulation over the northern hemisphere during June and October. Acta Meteorol Sin 29:249–263 (**in Chinese**)